INTERNATIONAL JOURNAL FOR NUMERICAL METHODS IN FLUIDS
Int. J. Numer. Meth. Fluids 2002; **38**:283–305 (DOI: 10.1002/fld.220)

Finite element study of free surface turbulent flow in rotating channels

Krishnan V. Pagalthivarthi*,† and Veeraraghavan Ramanathan[1]

Department of Applied Mechanics, Indian Institute of Technology, Hauz Khas, New Delhi 110016, India

SUMMARY

Under certain conditions of liquid flow through rotating channels, the Coriolis force can induce a free surface to be formed. This problem is of practical importance in a Coriolis wear tester, which is used for determining the sliding wear coefficient of wear materials in slurry handling equipment. A deforming Galerkin finite element method is presented for predicting two-dimensional turbulent free surface mean flow in rotating channels. Reynolds-averaged Navier–Stokes (RANS) equations are cast into weak (algebraic) form using primitive variables (velocity and pressure). Eddy viscosity is determined via a mixing length model. Velocity is interpolated biquadratically, while pressure is interpolated bilinearly. The kinematic condition is used to form the Galerkin residual for the free surface. The free surface is represented by Hermite polynomials of zeroeth order for continuity of position and slope. Combined Newton's iteration is used to simultaneously solve for the free surface and the field variables. Results of velocity and pressure fields, as well as the free surface are shown to converge with mesh-size refinement. There is excellent respect for mass conservation. Results are presented for various values of Rossby number (Ro) and height-based Reynolds number (Re_H). Parameter continuation in Ro and Re_H space is used to compute solutions at higher values of flow rate and angular velocity. Copyright © 2002 John Wiley & Sons, Ltd.

KEY WORDS: deforming mesh; free surface; rotating channel; finite element; mixing length model

1. INTRODUCTION

A large number of problems involving free surface flows have been reported in the literature. Such problems are encountered in, for example, movements of oceans and rivers, capillary flows, crystal growth, coating and polymer technology, die casting, liquid flows in partially filled pipes and channels, seepage flow and so forth. Several authors [1–3] have discussed typical free surface flow problems and methods used to solve them.

The problem of free surface flow in rotating channels is encountered in the Coriolis wear tester [4, 5], which is of significance to the slurry transportation industry. Although a number

---

*Correspondence to: K. V. Pagalthivarthi, Department of Applied Mathematics, Indian Institute of Technology, Hauz Khas, New Delhi, 110016, India.

†E-mail: kvp@am.iitd.ernet.in

[1] Now at University of Pennsylvania.

Received 25 September 2000
Revised 15 May 2001

of numerical [6–9] and experimental [10, 11] studies of flow through rotating channels are reported in the literature, to the authors' knowledge, none of them deals with viscous free surface flows.

In Figure 1, a typical setup of the Coriolis tester apparatus is shown. It consists of a rotating bowl with four detachable arms protruding radially out of it. The arms are hollow, machined, corrosion-resistant stainless steel tubes (of rectangular cross-section) which contain wear-resistant urethane molds within them. The mold has a 'T' shaped slot to accommodate the wear specimen. The longitudinal section of the Coriolis wear tester rotating channel is shown in Figure 1(b). Note that the wear sample is placed some distance downstream of the inlet to account for entrance effects. The relative flow (with respect to the rotating channel) has no entrance swirl. The wear specimen is placed vertically within the urethane mold as shown in Figure 1(c). Due to the rotation of the channel, a free surface may be formed for certain combinations of flow rate and rotation rate. Typically, the bowl has a rotation speed of 500–1000 rpm, and flow rate per channel ranges from 200–450 $\mathrm{cm}^3\,\mathrm{s}^{-1}$. The details of the slurry used in the test are discussed elsewhere [5]. Water (slurry) is pumped from a large tank into the rotating bowl. The flow rate can be adjusted by controlling the speed of the pump. As the bowl rotates, water (slurry) enters each of the four sample holders and flows along the channel. The outflow from the channel is collected in a trough and recycled through the wear tester. Since the primary interest in this paper is the free surface flow of the single-phase carrier liquid through rotating channels, discussion pertaining to two-phase flow is not included. The flow field computation of the carrier-phase liquid (usually water) is often an important first step in the numerical prediction of multiphase solid–liquid mixture flow field in slurry handling equipment [12].

The essential feature of the Coriolis wear tester relevant to the present work is a channel rotating about the z-axis as shown in Figure 2. Flow enters the channel through the inlet plane ADHE and exits to the atmosphere through the plane BCGF. As the channel rotates about the z-axis, the fluid surface DHCG contacting the channel wall detaches due to the Coriolis force, and becomes the free surface, DHC'G'. The extent of deflection of the free surface depends on the Rossby number and the height-based Reynolds number (Re_H). The actual free surface must be determined as part of the solution for specified values of the operating parameters.

As a first approximation, the flow is assumed to be two-dimensional through the mid-plane of the channel (parallel to the x–y plane). Since the primary focus here is to bring out the free surface effects, a mixing-length-type model is used for the turbulent viscosity. However, the methodology developed here is general enough to accommodate more comprehensive turbulent models in the future for further study.

The general method follows some of the earlier works [1, 2], with the following notable exceptions. Firstly, in sharp contrast to the previous works [1, 2], in the present work, the role of surface tension is negligible. It is the competition between centrifugal and Coriolis forces (which vary with spatial location) that induces the formation of the free surface. Secondly, the previous applications were for slowly moving flows as is characteristic in coating, polymer processing, and steady vertical solidification. In the present application, it is the opposite extreme, which is of interest. The channel height-based Reynolds number is of the order of $10\,000 \sim 50\,000$ for most cases, which not only makes the inertial forces important, but also puts the flow in the turbulent regime. Furthermore, the formation of free surface forces the liquid (to maintain continuity) to speed up as it traverses the channel. This further increases the local Reynolds number downstream of the channel inlet. Thus, both kinds of non-linearity—

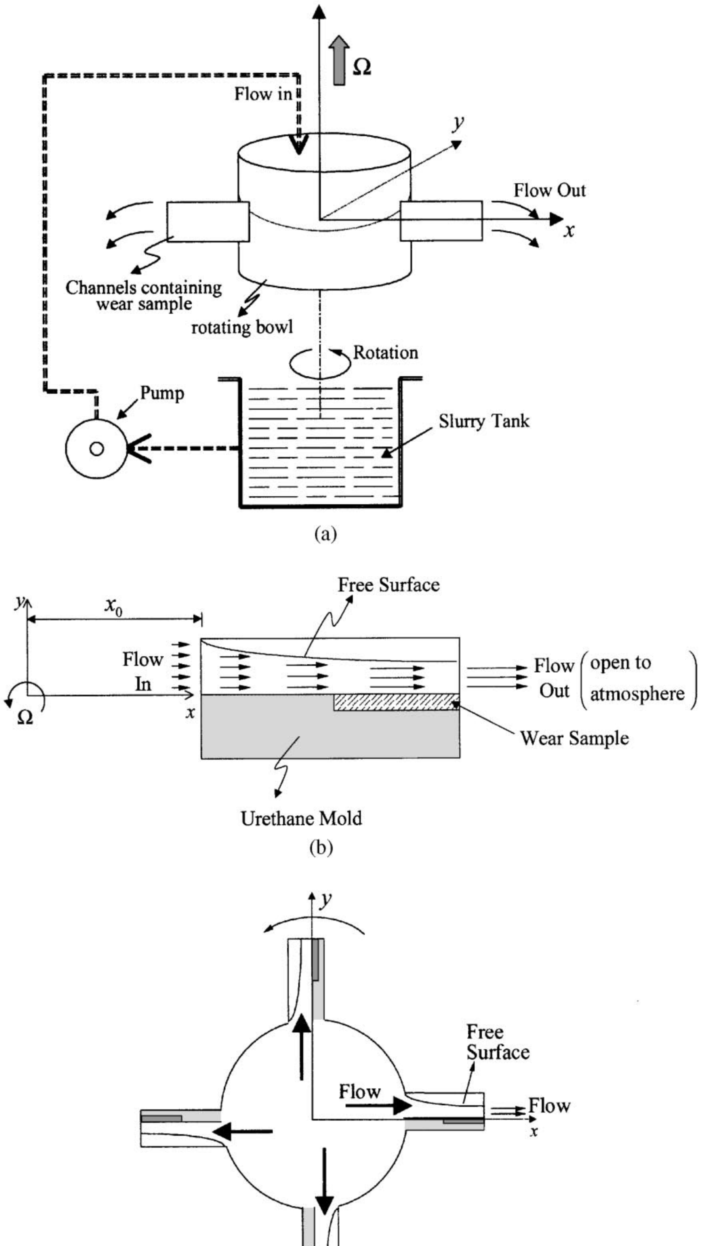

Figure 1. Schematic diagrams of (a) full set-up of Coriolis wear tester [5], (b) cross-section of channel showing wear sample and free surface flow (c) sectional view of bowl.

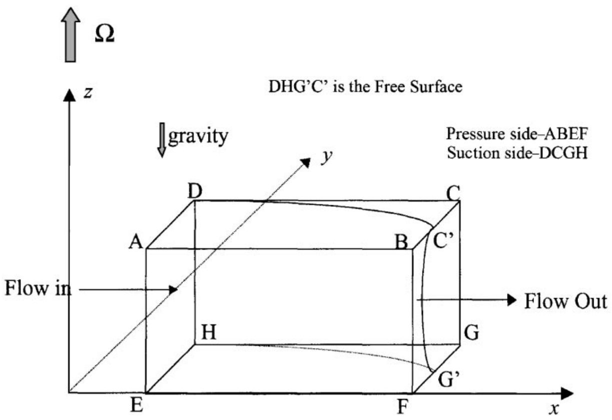

Figure 2. Three-dimensional schematic diagram of rotating channel flow with free surface.

one due to the unknown free surface and the other due to the nonlinear RANS equations governing the flow field—are important in the present problem.

For ease of implementation, the free surface is modeled as zeroeth order Hermite polynomials. This allows for slope continuity in addition to the usual continuity of position. Such an idea has previously been applied [13] to moving boundary problems in solidification with a discrete unknown solid–liquid interface. The same idea has been extended [14] to alloy solidification with unknown solid–mush and liquid–mush interfaces. Since the free surface does not become a multi-valued function of the x-coordinate, the choice of Hermite polynomials to represent the free surface is found to be adequate for the present problem.

For large flow Reynolds number, a useful approximation may be obtained by assuming the flow field relative to the rotating reference frame to be inviscid and irrotational. In such an approximation, a stream function (satisfying Laplace's equation) may be introduced to compute the flow field, restricting the non-linearity to the free surface alone. This has been successfully done [15] for the range of Rossby number encountered in the Coriolis wear tester. This method is extended here to the prediction of two-dimensional viscous (turbulent) free surface flow in rotating channels.

2. GOVERNING EQUATIONS

Consider the two-dimensional free surface flow configuration shown in Figure 1(b). The x–y coordinate axes are attached to the rotating channel. Let $\vec{u}$ $(=u\hat{\imath}+v\hat{\jmath})$ be the mean flow velocity relative to the channel and ρ be the density of the incompressible liquid. By Reynolds-averaging the continuity and Navier–Stokes equations, the governing equations for the mean flow field in the rotating reference frame are written as

$$\nabla\cdot\vec{u}=0 \tag{1}$$

and

$$\rho(\vec{u}\cdot\nabla)\vec{u}=\nabla\cdot(\underset{\sim}{\tau}-p\underset{\sim}{I})-2\rho\vec{\Omega}\times\vec{u}-\rho\vec{\Omega}\times(\vec{\Omega}\times\vec{r}) \tag{2}$$

where $\vec{\Omega}$ $(=\Omega\hat{k})$ is the angular velocity of the channel, p is the pressure, $\vec{r}$ is the position vector $(=x\hat{i}+y\hat{j})$, and $\underset{\sim}{I}$ is the identity tensor. The last two terms in Equation (2) represent the Coriolis and centrifugal forces, respectively, due to the rotating frame of reference. The stress tensor $\underset{\sim}{\tau}$ is defined as

$$\tau_{ij}=(\mu+\mu_t)\left(\frac{\partial u_i}{\partial x_j}+\frac{\partial u_j}{\partial x_i}\right) \tag{3}$$

where μ and μ_t are the laminar and eddy viscosities, respectively.

A mixing length type of model is used to calculate the eddy viscosity as

$$\mu_t=\kappa\rho y\left(1-\frac{\alpha y}{S(x)}\right)\frac{\sqrt{u^2+v^2}}{A+B\log_{10}(y/r_w)} \tag{4}$$

where κ $(=0.4)$, α, A $(=5.98)$ and B $(=5.75)$ are constants, y is the distance from the wall $(y=0)$, $S(x)$ is the local height of the free surface and r_w is the wall roughness. An expression similar to Equation (4) has been used [16] to model eddy viscosity in pump impeller channels. When $\alpha\to 1$, for $y\to S$, the eddy viscosity approaches zero. The view that near the free surface the eddy viscosity tends to vanish is supported by other authors [17]. However, the adjustable value of α allows freedom to consider other possibilities.

The following non-dimensionalization of the variables is chosen:

$$\begin{aligned}(u^*,v^*)&=\frac{(u,v)}{U_0}\\ p^*&=\frac{p}{\rho U_0^2}\\ \Omega^*&=\frac{\Omega L}{U_0}=\frac{1}{Ro}\end{aligned} \tag{5}$$

and

$$(x^*,y^*)=\frac{(x,y)}{L}$$

where the asterisk $(^*)$ denotes non-dimensional quantities, U_0 is the uniform inlet velocity, L is the channel length and Ro is the Rossby number (reciprocal of rotation number, Ω^*). Introducing Equation (5) into Equations (1) and (2) and omitting the asterisk for convenience, the non-dimensional scalar form of Equations (1) and (2) may be written as

$$\frac{\partial u}{\partial x}+\frac{\partial v}{\partial y}=0 \tag{1a}$$

$$u\frac{\partial u}{\partial x} + v\frac{\partial u}{\partial y} = \Omega^2 x + 2\Omega v + \frac{\partial}{\partial x}\left\{\frac{2(1+\upsilon_r)}{Re}\frac{\partial u}{\partial x} - p\right\} + \frac{\partial}{\partial y}\left\{\frac{(1+\upsilon_r)}{Re}\left(\frac{\partial u}{\partial y} + \frac{\partial v}{\partial x}\right)\right\} \tag{6}$$

and

$$u\frac{\partial v}{\partial x} + v\frac{\partial v}{\partial y} = \Omega^2 y - 2\Omega u + \frac{\partial}{\partial x}\left\{\frac{(1+\upsilon_r)}{Re}\left(\frac{\partial u}{\partial y} + \frac{\partial v}{\partial x}\right)\right\} + \frac{\partial}{\partial y}\left\{\frac{2(1+\upsilon_r)}{Re}\frac{\partial v}{\partial y} - p\right\} \tag{7}$$

where $Re = \rho U_0 L/\mu$ is the length-based Reynolds number, and υ_r is the ratio μ_r/μ.

Boundary conditions are as follows. At the inlet ($x = x_0$), uniform parallel flow is assumed. At the impermeable pressure-side wall ($y = 0$), wall functions are used. Or alternately, no-slip may be used for the x-component of velocity. At the free surface ($y = S(x)$), the pressure and shear stress must vanish, and the normal stress must be equal to the pressure. This follows from the assumption that surface tension is negligible. In addition, the kinematic condition must be satisfied along the free surface, i.e., the free surface must be a streamline. For the exit boundary condition, the usual strategy of extended domain for flow through turbomachine rotors is adopted [18]. At the exit of the computational domain ($x = x_{\text{inlet}} + \text{channel length} + \text{extension length}$), zero-gradient conditions are imposed. An extension of about 20 per cent of the channel length is found to be adequate for the present problem. Thus, the exit of the channel is at $x = x_0 + 1.2$ (non-dimensional units), where x_0 is the location of the channel entrance.

In non-dimensional form, the boundary conditions are

$$\text{Along } x = x_0, \quad 0 < y < H: \quad u = 1, \quad v = 0 \tag{8}$$

$$\text{Along } y = 0, \quad x_0 \leqslant x \leqslant x_0 + 1.2: \quad u = 0, \quad v = 0 \tag{9}$$

The no-slip condition at the wall may, alternately, be replaced by the 'law of the wall' for rotating passages [19] as

$$u^+ = \begin{cases} \dfrac{1}{\kappa}\ln(Ey^+) + \dfrac{2\beta\Omega y}{u_\tau} & \text{for } y^+ \geqslant 11.6 \\ y^+ & \text{for } y^+ < 11.6 \end{cases} \tag{9a}$$

where κ ($\cong 0.4$) and E ($\cong 9.8$ for smooth wall) are constants. The non-dimensional velocity, u^+, is defined as u/u_τ and $y^+ = yu_\tau/v$ is the non-dimensional distance from the wall. Here u_τ is the friction velocity. The parameter β is the Monin–Oboukhov coefficient [19]. Based on detailed experiments, β is found to fit the correlation [20]:

$$\beta = \begin{cases} 1.25 - 1.73Ro_x : Ro_x < 0.4 \\ 3.07\sqrt{|Ro_x|} \quad : -0.4 \leqslant Ro_x \leqslant 0 \\ 1.91\sqrt{Ro_x} \quad : 0 \leqslant Ro_x \leqslant 0.4 \\ 0.71 + 1.24Ro_x : 0.4 < Ro_x \end{cases} \tag{9b}$$

where $Ro_x = [(\Omega x)/(U_\delta)]$ is the local Rossby number, U_δ being the free stream velocity at x.

Note that $y^+ < 11.6$ corresponds to the laminar sublayer and hence is not corrected for rotation effect in this region.

$$\text{Along } x = x_0 + 1.2, \quad 0 < y < S(x_0 + 1.2): \quad \frac{\partial u}{\partial x} = 0, \quad \frac{\partial v}{\partial x} = 0 \tag{10}$$

and

$$\begin{gathered}\text{along the free surface,} \quad y = S(x), \quad x_0 < x < x_0 + 1.2: \\ \tau_{nn} = p = 0, \quad \tau_{nt} = 0 \quad \text{and} \quad \vec{u} \cdot \hat{n} = 0\end{gathered} \tag{11}$$

where, τ_{nn} and τ_{nt} are the normal and tangential stresses, and $\hat{n}$ is the unit outward normal to the free surface. The first two conditions in Equation (11) are the dynamic conditions while the third is the kinematic condition.

In the limit of large Re, the inviscid approximation to Equations (1a), (6) and (7) is valid. This special case has been dealt with elsewhere [15] via a stream function approach.

3. FINITE ELEMENT FORMULATION

The free surface in the rotating channel is a single-valued function of distance along the channel. Deforming mesh finite element method for steady solidification of metals [13] and alloys [14], and for inviscid free surface flow in rotating channels [15] is extended here to viscous (turbulent) free surface flow in a rotating channel.

The problem domain is discretized using nine-noded isoparametric quadrilateral elements (Figure 3). The free surface is approximated by Hermite cubic polynomials of zeroeth order to preserve continuity of slope and position of the free surface. There are as many Hermite elements on the free surface as there are biquadratic elements in the x-direction. Thus, the height, $S_e(\xi)$, of the free surface at an arbitrary value of the normalized coordinate, $\xi \in [-1, 1]$

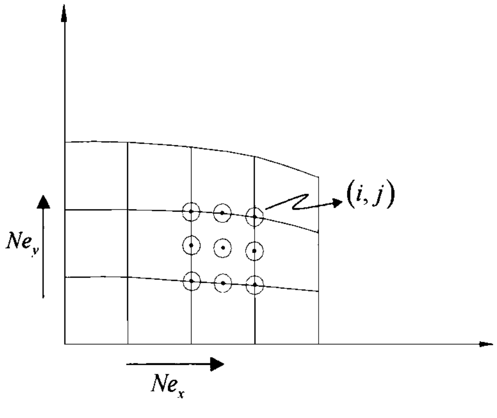

Figure 3. A typical finite element mesh for the problem domain.

is given by

$$S_e(\xi) = \sum_{i=1}^{4} H_i(\xi) a_i \tag{12}$$

where $H_i(\xi)$ are the Hermite polynomials and a_i are coefficients defined as

$$a_1 = S_e(-1), \quad a_2 = \frac{\partial S_e(-1)}{\partial x}, \quad a_3 = S_e(1) \quad \text{and} \quad a_4 = \frac{\partial S_e(1)}{\partial x} \tag{13}$$

The inviscid solution [15] is used as the initial guess for the free surface to generate the initial mesh. The coordinates of any corner node (i,j) of an element are determined as

$$x_{ij} = \frac{i-1}{Ne_x} \quad \text{and} \quad y_{ij} = \frac{(j-1)S(x_{ij})}{Ne_y} \tag{14}$$

The y-coordinates of the nodes thus depend on the free surface, and are updated at every iteration. In Equation (14), uniform mesh is assumed, although grading is possible in either direction. The coordinates of the midside (and body centred) nodes are calculated by interpolation of the corner nodes.

Velocity components are interpolated biquadratically (N_i) and pressure is interpolated bilinearly (N_{p_i}) within each element. The standard Galerkin weighted residual method is applied at the element level to Equations (1a), (6) and (7). After application of Green's theorem to the viscous terms, the Galerkin residuals are

$$R_{p_i} = \int_{-1}^{1}\int_{-1}^{1} N_{p_i}\left(\frac{\partial u}{\partial x} + \frac{\partial v}{\partial y}\right)|J|\,\mathrm{d}\xi\,\mathrm{d}\eta \tag{15}$$

$$R_{u_i} = \int_{-1}^{1}\int_{-1}^{1} \begin{bmatrix} N_i\left(u\dfrac{\partial u}{\partial x} + v\dfrac{\partial u}{\partial y} - \Omega^2 x - 2\Omega v\right) \\ +\dfrac{\partial N_i}{\partial x}\left\{\dfrac{2(1+\upsilon_r)}{Re}\dfrac{\partial u}{\partial x} - p\right\} \\ +\dfrac{\partial N_i}{\partial y}\dfrac{(1+\upsilon_r)}{Re}\left(\dfrac{\partial u}{\partial y} + \dfrac{\partial v}{\partial x}\right) \end{bmatrix} |J|\,\mathrm{d}\xi\,\mathrm{d}\eta - \int_{\Gamma_2^{(e)}} N_i \left\{ \begin{matrix} (\tau_{xx} - p)n_x \\ + \tau_{xy} n_y \end{matrix} \right\} \mathrm{d}\Gamma_2^{(e)} \tag{16}$$

and

$$R_{v_i} = \int_{-1}^{1}\int_{-1}^{1} \begin{bmatrix} N_i\left(u\dfrac{\partial v}{\partial x} + v\dfrac{\partial v}{\partial y} - \Omega^2 y + 2\Omega u\right) \\ +\dfrac{\partial N_i}{\partial x}\dfrac{(1+\upsilon_r)}{Re}\left(\dfrac{\partial u}{\partial y} + \dfrac{\partial v}{\partial x}\right) \\ +\dfrac{\partial N_i}{\partial y}\left\{\dfrac{2(1+\upsilon_r)}{Re}\dfrac{\partial v}{\partial y} - p\right\} \end{bmatrix} |J|\,\mathrm{d}\xi\,\mathrm{d}\eta - \int_{\Gamma_2^{(e)}} N_i \left\{ \begin{matrix} (\tau_{yy} - p)n_y \\ + \tau_{xy} n_x \end{matrix} \right\} \mathrm{d}\Gamma_2^{(e)} \tag{17}$$

In Equations (15)–(17) $|J|\,\mathrm{d}\xi\,\mathrm{d}\eta=\mathrm{d}x\,\mathrm{d}y$ is the element differential volume (area), $\Gamma_2^{(e)}$ is that part of the element boundary which coincides with the domain boundary with stress boundary conditions, and n_x and n_y are the components of the outward normal to Γ_2. The determinant $|J|$ is the Jacobian of the transformation $(x,y)\rightarrow(\xi,\eta)$ from Cartesian (global) to normalized (local) coordinates.

Along the free surface, the first two conditions of Equation (11) may be shown to imply that the boundary terms in Equations (16) and (17) must vanish. At the exit, $n_x=1$ and $n_y=0$ along with Equation (10) reduces the boundary integral in Equations (16) and (17) to

$$\int_{-1}^{1} N_i p \frac{\partial y}{\partial \eta}\,\mathrm{d}\eta$$

and

$$\int_{-1}^{1} \frac{N_i(1+\upsilon_r)}{Re}\frac{\partial u}{\partial y}\frac{\partial y}{\partial \eta}\,\mathrm{d}\eta$$

respectively.

The residuals in Equations (16) and (17) depend on the element area, which in turn depends on the free surface parameters, a_i. Likewise, the partial derivatives such as $(\partial u/\partial x)$, $(\partial u/\partial y)$ etc. depend on the free surface parameters. For a given (assumed) set of a_i, the nonlinear algebraic Equations (15)–(17) may be solved to determine the nodal values of u, v and p. In the combined Newton's method, the field variables u, v, p and the free surface parameters are determined by simultaneous iteration for both [13–15]. The free surface residual is formed using the thus far unused kinematic condition $\vec{u}\cdot\hat{n}=0$ in Equation (11). Using the Hermite polynomials, H_i, as weighting functions, the free surface residual is given as

$$R_{a_i}=\int_{-1}^{1} H_i\left(u\frac{\mathrm{d}y}{\mathrm{d}x}-v\right)\sqrt{1+\left(\frac{\partial S}{\partial x}\right)^2}\,\frac{\partial x}{\partial \xi}\,\mathrm{d}\xi \tag{18}$$

where

$$\sqrt{1+\left(\frac{\partial S}{\partial x}\right)^2}\,\frac{\partial x}{\partial \xi}\,\mathrm{d}\xi=\sqrt{1+\left(\frac{\partial S}{\partial x}\right)^2}\,\mathrm{d}x=\mathrm{d}\Gamma^{(e)}$$

is a differential length element along the free surface.

Let $\underset{\sim}{X}=(\underset{\sim}{u}^T\ \underset{\sim}{v}^T\ \underset{\sim}{p}^T\ \underset{\sim}{a}^T)^T$ be the vector of nodal values of u, v, p and the free surface parameters $\underset{\sim}{a}$. The corresponding vector of residuals is denoted by $\underset{\sim}{R}_k=(\underset{\sim}{R}_u^T\ \underset{\sim}{R}_v^T\ \underset{\sim}{R}_p^T\ \underset{\sim}{R}_a^T)^T$. The superscript T denotes the transpose operator. In the combined Newton's iteration, the correction vector $\delta\underset{\sim}{X}^{(k)}$ at the kth iteration is obtained by solving the linear system

$$[Q]\delta\underset{\sim}{X}^{(k)}=-\underset{\sim}{R}_X \tag{19}$$

where the Jacobian matrix $[Q]$ is given as

$$[Q]=\frac{\partial \underset{\sim}{R}_X}{\partial \underset{\sim}{X}} \tag{20}$$

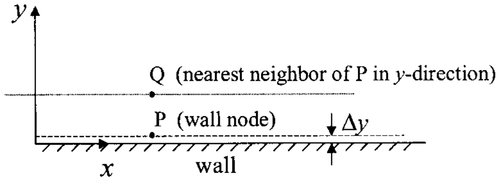

Figure 4. Location of wall node and its neighbor.

The vector $\underset{\sim}{X}$ is then updated as

$$\underset{\sim}{X}^{(k+1)} = \underset{\sim}{X}^{(k)} + \delta\underset{\sim}{X}^{(k)} \tag{21}$$

If necessary, under-relaxation may be incorporated into Equation (21) for convergence.

The derivatives in the $[Q]$ matrix are determined analytically. Although tedious, this straightforward step, detailed elsewhere [21], is not included here.

The linear system (Equation (19)) is solved for $\delta\underset{\sim}{X}^{(k)}$ using the frontal method [22], employed very commonly in finite element practice. One modification was done to the basic frontal algorithm to efficiently use the large random access memory (RAM) available on our machine. During elimination, instead of writing the pivotal information for each equation to the hard disk, this information is stored in an allocatable (dynamic) array. This strategy boosts up the performance by two to three times, depending on the machine configuration.

While using the 'law of the wall' boundary conditions, an iterative procedure is used to specify the slip velocity at the wall. Referring to Figure 4, node P corresponds to the wall, while node Q corresponds to the nearest adjacent node, just clearing the wall in the y-direction. For any iteration, k, (in Equations (19)–(21)) let $u_Q^{(k)}$ and $u_P^{(k)}$ be the x-components of velocity at points Q and P, respectively. The tentative friction velocity, u_τ, corresponding to u_Q is determined by iteratively solving Equation (9a). With this calculated value of u_τ, the velocity $u_P^{(k+1)}$ is determined by using Equation (9a) again with $y = y_P$. For this purpose, the wall node P is displaced a small arbitrary distance (shown dotted), taken as $\Delta y = 0.0005$ in this study. A graded mesh is typically essential to maintain Q within the log-layer of the boundary. For the $(k+1)$st iteration, $u_P^{(k+1)}$ is used as the prescribed velocity at node P. This procedure is repeated for all nodes along the wall.

The introduction of wall functions results in the loss of quadratic convergence property of Newton's method (Equation (19)). Thus, the number of combined Newton's iterations typically increases by a factor of two to three times for convergence to the same tolerance.

4. RESULTS AND DISCUSSION

All computations in this study were performed on a 466MHz Pentium II® with 512 MB RAM. Mesh refinement studies were carried out using 100 × 10, 150 × 15 and 200 × 10 elements for $Re_H = 19\,685$, $Ro(U_0/\Omega L) = 0.466$, aspect ratio, $H/L = 0.1$, and inlet location at $x_0 = 1.7$. These values are typical in the Coriolis wear tester channel. In order to capture the sharp velocity gradient at the channel base, the mesh is graded in the y-direction by appropriate stretching

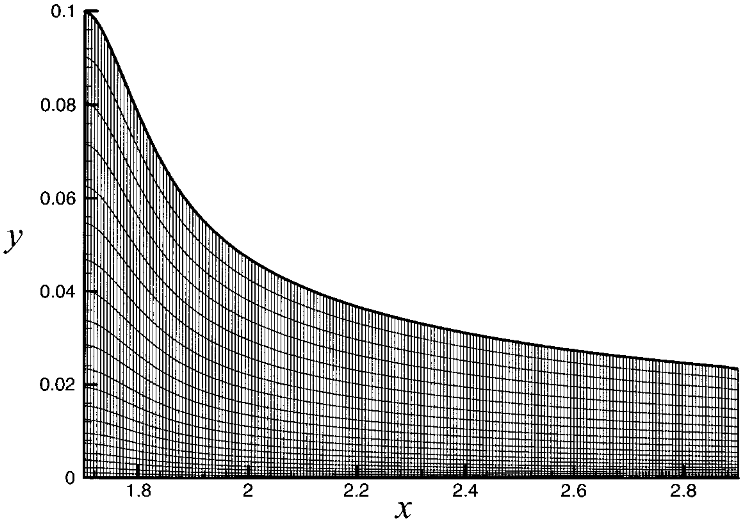

Figure 5. 100 × 10 graded mesh for converged solution of Case 4 of Table I.

[23]. In Figure 5, the converged 100 × 10 graded mesh is shown to give an idea of the level of grading. The results of the mesh refinement computations are summarized in Figure 6 in the form of velocity and pressure profiles, and mass conservation.

The velocity and pressure profiles at $x = x_0 + 1/3$, $x_0 + 2/3$ and $x_0 + 1$ are very close for all three meshes. Mass loss plotted in Figure 6(c) is calculated as

$$\% Q_{\text{loss}} = \% \,\text{Mass lost at } x = \frac{(\int_0^H u\,\mathrm{d}y)_{\text{inlet}} - (\int_0^{S(x)} u\,\mathrm{d}y)_{\text{at } x}}{(\int_0^H u\,\mathrm{d}y)_{\text{inlet}}} \tag{22}$$

The results for the 150 × 15 mesh are only slightly better than those for the 100 × 10 or 200 × 10 meshes. The results for 100 × 10 and 200 × 10 meshes nearly coincide. The flow conditions used for the mesh refinement study are very stringent in terms of solution convergence. Hence either the 150 × 15 or 200 × 10 mesh is considered adequate for all other cases studied. Since the 150 × 15 mesh, due to its higher front width, requires about 50 per cent larger computation time than the 200 × 10 mesh, the latter is preferred. Five to six iterations are required for overall convergence. The solution is considered converged when

$$\|\delta \underset{\sim}{X}^{(k)}\|_\infty < 10^{-8} \tag{23}$$

i.e., the infinity norm of the correction vector is less than a tolerance of 10^{-8}.

In Table I, a list of finite element solutions obtained is shown. In all cases, overall mass conservation is satisfied excellently. In Figures 7 and 8 velocity and pressure fields are shown for Cases 1–4 of Table I. In all cases, Re_H, H/L and x_0 are kept constant, while the Rossby number, Ro, is decreased (Ω is increased). For relatively large Ro, the free surface deflects only slightly. As Ro is decreased, the free surface deflection increases and so does the exit velocity. For $Ro = 0.259$, the exit velocity is six to seven times the inlet velocity. There is

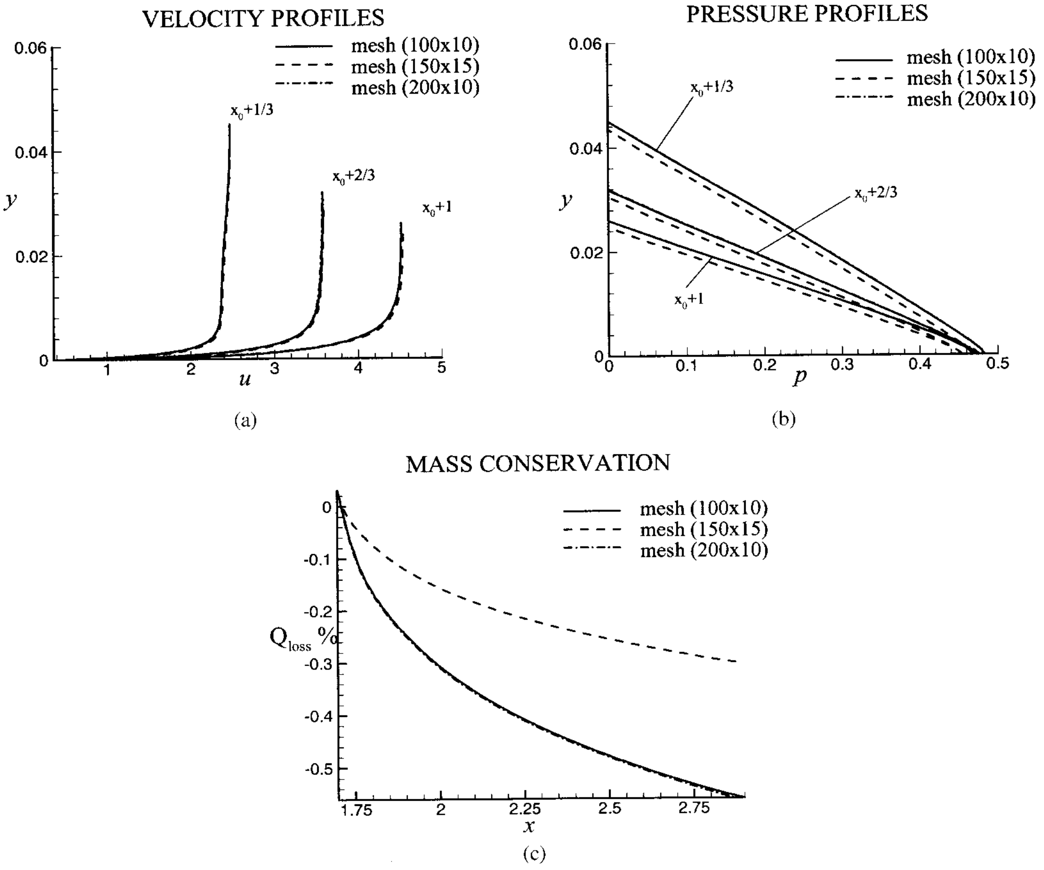

(a) (b) (c)

Figure 6. Effect of mesh refinement on (a) velocity profiles, (b) pressure profiles and (c) mass conservation.

a significant increase in velocity gradient (shear stress) at the wall. The average pressure gradient is seen to vary as $-2\Omega u$ in all cases. This indicates that the transverse pressure gradient is primarily due to the Coriolis acceleration.

In Figure 9, inviscid computations [15] are compared with the present turbulent flow field computations for Case 4 of Table I. Outside the boundary layer (adjacent to $y=0$), the velocity in the free stream predicted by the turbulent code is smaller than the inviscid code prediction. The free surface height at exit for the turbulent case is about 20 per cent higher in comparison with the inviscid case. Likewise, higher pressures are predicted by the turbulent code. Damping due to viscous effects is the obvious explanation for these differences. However, the general trends predicted by both the inviscid and turbulent codes are similar.

In Figure 10, free surface profiles are shown for several values of *Ro* (Cases 1–4 of Table I). The free surface deflection is not linearly proportional to *Ro*. For smaller *Ro*, there is a steep fall in the free surface near the entrance.

Table I. Finite element solutions for turbulent flow using 200×10 mesh.

Case	Ω (rpm)	Ro	H/L	x_0	Re_H	Q ($\text{m}^3\,\text{s}^{-1}$)	$\dfrac{100(Q_{\text{in}} - Q_{\text{out}})}{Q_{\text{in}}}$
1	200	1.294	0.056	0.944	19 685	2.5×10^{-4}	−0.18%
2	500	0.518	0.056	0.944	19 685	2.5×10^{-4}	−0.44%
3	750	0.345	0.056	0.944	19 685	2.5×10^{-4}	−0.59%
4	1000	0.296	0.056	0.944	19 685	2.5×10^{-4}	−0.72%
5	1000	0.466	0.1	1.7	19 685	2.5×10^{-4}	−0.58%
6	1000	0.512	0.056	0.944	39 370	5.0×10^{-4}	−0.48%
7	1000	0.256	0.056	0	19 685	2.5×10^{-4}	−0.55%
8	1000	0.780	0.056	0.944	59 055	7.5×10^{-4}	−0.35%
9	1000	1.040	0.050	0.944	78 740	1.0×10^{-3}	−0.27%

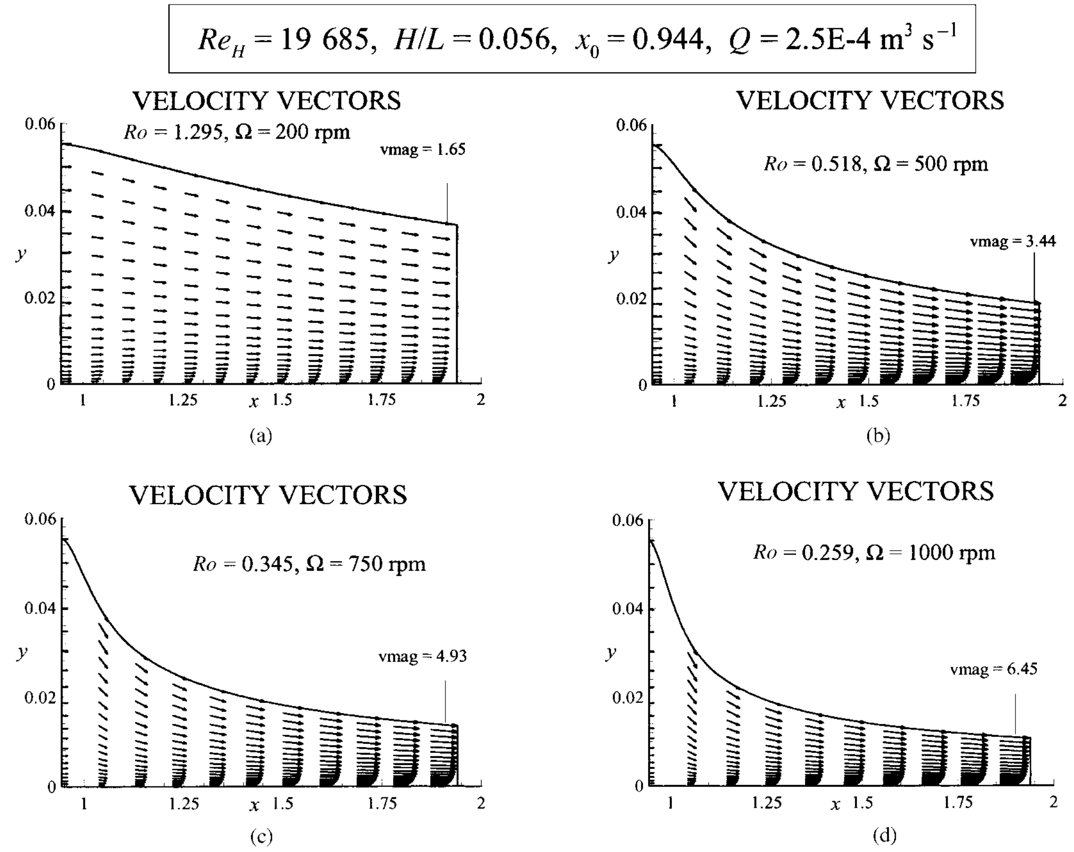

(a) (b) (c) (d)

Figure 7. Comparison of velocity field from turbulent finite element solutions for (a) Case 1, (b) Case 2, (c) Case 3 and (d) Case 4 of Table I.

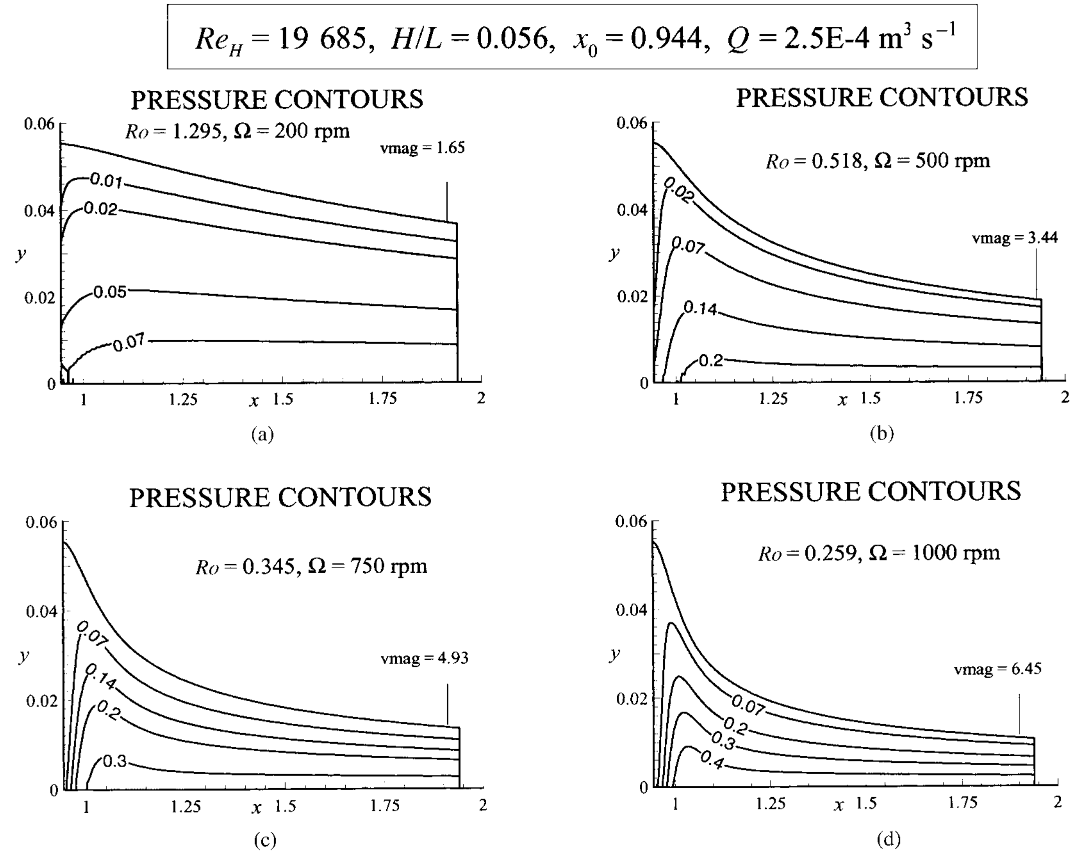

(a) (b)

(c) (d)

Figure 8. Pressure field from turbulent finite element solutions for (a) Case 1, (b) Case 2, (c) Case 3 and (d) Case 4 of Table I.

In general, the deflection of the free surface depends not only on the rotation rate (or Ro) but also on the flow rate (or Re_H). In Figures 11 and 12 the effect of varying Re_H at constant Ω ($= 1000$ rpm) is shown. As the flow rate is increased at constant Ω, the free surface deflection decreases and so does the ratio of the exit to inlet velocity. In Figures 11 and 12, although the non-dimensionalized exit velocity decreases with increasing Q (Re_H), the dimensional exit velocity increases from $19.96\ \text{m}\ \text{s}^{-1}$ for $Q = 2.5\times 10^{-4}\ \text{m}^3\ \text{s}^{-1}$ to $23.56\ \text{m}\ \text{s}^{-1}$ for $Q = 10.0\times 10^{-4}\ \text{m}^3\ \text{s}^{-1}$. Similarly, the actual pressures are higher as Q increases. For example, the maximum pressure for $Q = 2.5\times 10^{-4}\ \text{m}^3\ \text{s}^{-1}$ is $4613\ \text{N}\ \text{m}^{-2}$ and for $Q = 10.0\times 10^{-4}\ \text{m}^3\ \text{s}^{-1}$, it is $16914.3\ \text{N}\ \text{m}^{-2}$.

The velocity adjacent to the wall ($y = 0$) is an important parameter that determines sliding wear (in case of slurry flow). In Figure 13(a), the velocity along the wall is shown as a function of x for Cases 1–4 of Table I; and in Figure 13(b) the velocity at a distance of 1 per cent of the free surface height ($y/y_{fs} \cong 0.01$) from the channel base is shown. At the

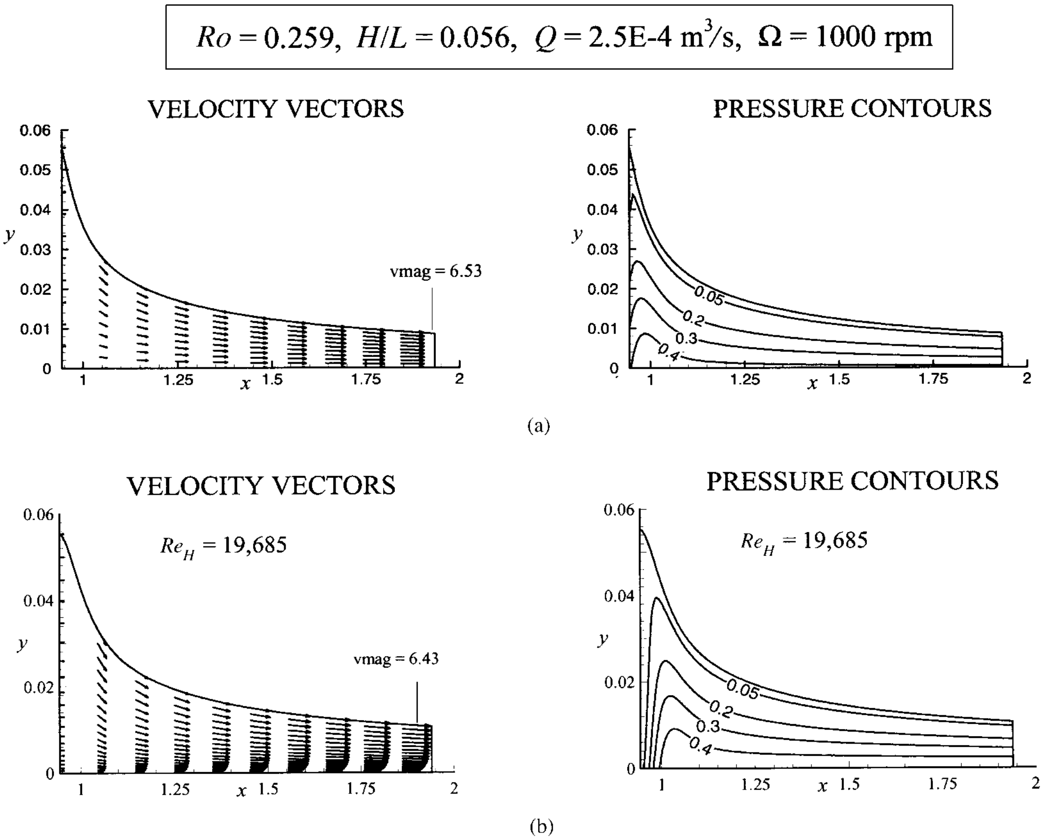

Figure 9. Comparison of (a) inviscid and (b) turbulent flow fields for Case 4 of Table I.

channel inlet, in Figure 13(b), the flow adjacent to the wall at ($y/y_{fs} \cong 0.01$) tends to initially decelerate due to the wall friction. Thereafter, the formation of free surface causes the free stream velocity and hence the velocity adjacent to the wall to increase. In contrast, for flow over a flat plate, the velocity adjacent to the wall continues to decrease asymptotically. As the angular velocity is increased, the free surface deflects more (due to increased Coriolis force), the free stream velocity increases and so does the near-wall velocity.

The velocity at the wall, (node P of Figure 4) does not indicate an initial deceleration. After an initial somewhat steep increase in velocity, the acceleration is more or less constant. This again corroborates with the initial steep fall in the free surface, especially at higher values of Ω.

Turbulent boundary layer properties are compared for $\Omega = 200$ rpm and $Q = 1000$ rpm in Figure 14. The boundary layer thickness, δ, is defined as the distance from the wall at which the streamwise velocity attains 99 per cent of its free stream value. This is calculated by interpolation of the velocity between grid points. The wall shear stress is computed using Equation (9b), i.e. logarithmic 'law of the wall'. Due to the fine grading of the mesh near

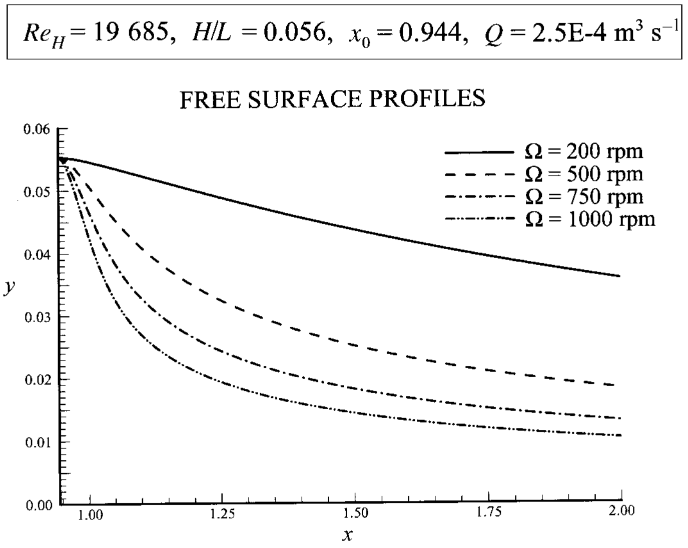

Figure 10. Effect of angular velocity on free surface profile.

the base of the channel, we expect these results to be fairly accurate. Furthermore, the use of the logarithmic law ensures reasonable accuracy in the wall shear stress.

Apart from the quantitative accuracy, the qualitative trends shown are new results, not found (to our knowledge) in the open literature. Hopefully, these results will attract a new avenue of interest in this class of problems. The qualitative trends observed here are physically plausible, and give valuable insight into the physics of the problem.

In Figure 14, the channel entrance is at the origin ($x_0 = 0$). In the numerical calculations, there is a significant difference between u_Q and u_P (Figure 4) at $x = x_0$. Thus, the boundary layer thickness at the entrance is not zero (as is customarily taken in analytical calculations). For the same reason, the shear stress at $x = 0$ is not zero. Thus, the shear stress initially decreases, before beginning to increase. As the rotation rate increases, the boundary layer thickness decreases due to the cross-stream pressure gradient set up by the Coriolis force. Correspondingly, there is an increase in wall shear stress, τ_w as Ω increases. After some initial distance, the shear stress also increases with x due to the increasing Coriolis acceleration ($2\Omega u$). As shown in Figure 1(b), in the Coriolis wear tester channel, the wear sample is placed a certain distance downstream of the channel. Thus, the wear sample falls within the region of increasing shear stress.

In the actual Coriolis wear tester, wear depth on the sample is seen to increase with x [24]. This is corroborated by the increasing wall shear and near-wall velocity predicted by the present study.

As a matter of curiosity, in Figure 15, the velocity and pressure profiles are compared for the cases of no-slip and log-law along the base of the channel. As expected, the velocity profiles are somewhat steeper with the 'law of the wall' boundary conditions. The predicted pressures are likewise lower for the no-slip case, corresponding to the lower velocities.

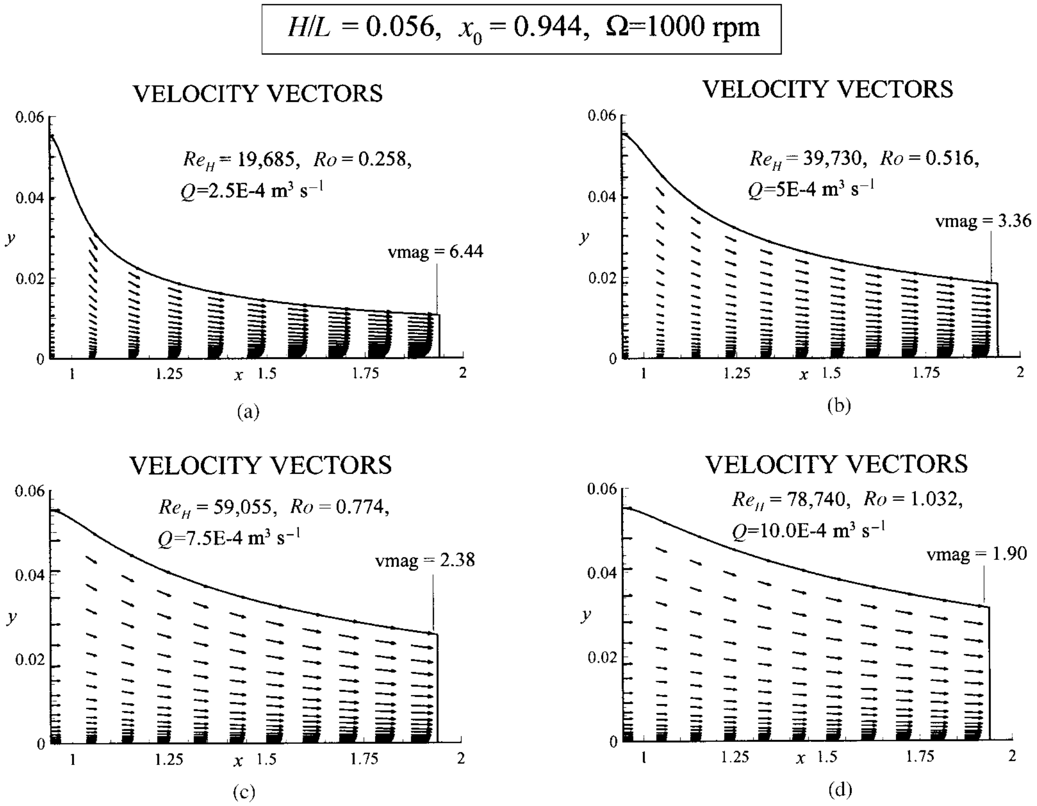

Figure 11. Comparison of non-dimensional velocity vectors at constant $\Omega = 1000$ rpm for (a) $Q = 2.5\,\mathrm{E}-4$, (b) $Q = 5.0\,\mathrm{E}-4$, (c) $Q = 7.5\,\mathrm{E}-4$ and (d) $Q = 10.0\,\mathrm{E}-4\,\mathrm{m}^3\,\mathrm{s}^{-1}$, respectively.

5. CONCLUDING REMARKS

The deforming mesh Galerkin finite element method used in this study has previously been used in solidification and film coating studies where the flow rates are small in a non-rotating reference frame. The present application to free surface flow in rotating channels involves flow velocities in the turbulent regime, along with the additional complications introduced by the rotating frame of reference. Considering these extra complications involved in this, we adopt a simple mixing length model to account for turbulence, since our primary interest here is to study the free surface effects.

The free surface is modeled using Hermite elements to maintain continuity of slope and position. The kinematic condition at the free surface is used to form the free surface residual. A combined Newton's iteration is used to simultaneously solve for the field variables and free surface.

The method turns out to be very efficient for predicting this class of free surface flows. Within five to six combined Newton's iterations, a converged solution is obtained for a given set of parameters for the no-slip boundary conditions; for wall functions 12–15 iterations are

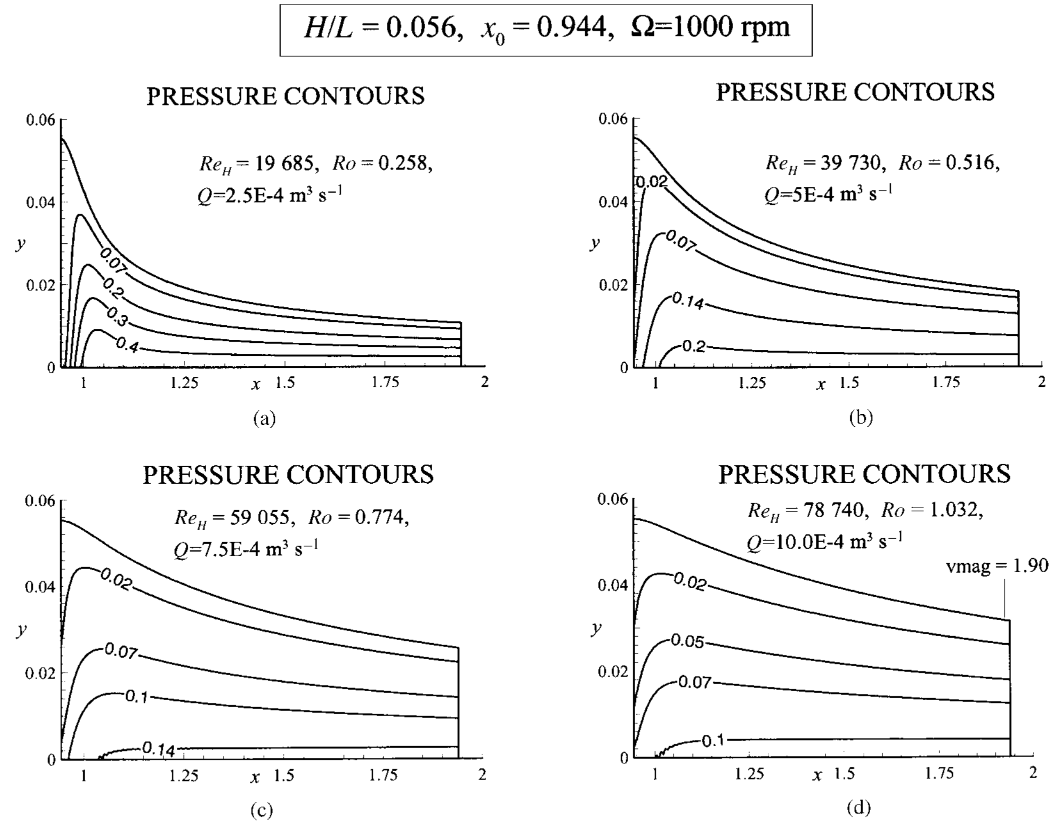

Figure 12. Comparison of non-dimensional pressure contours at constant $\Omega = 1000$ rpm for (a) $Q = 2.5\,\mathrm{E} - 4$, (b) $Q = 5.0\,\mathrm{E} - 4$, (c) $Q = 7.5\,\mathrm{E} - 4$ and (d) $Q = 10.0\,\mathrm{E} - 4\,\mathrm{m}^3\,\mathrm{s}^{-1}$, respectively.

required. With the basic methodology established, it is possible to consider a more comprehensive turbulence model such as the κ–ε model, including modifications for rotation effects.

The performance of a more comprehensive turbulence model would again depend upon: (i) the modification(s) introduced for Coriolis correction; (ii) the use of proper wall functions; and (iii) the degree of mesh refinement near the channel base. Of these three factors, (ii) and (iii) are adequately accounted for even in the present study. Comparison of solutions with and without wall functions (Figure 15) shows that the general trend of the velocity profiles are similar for the two cases. Indeed, with wall functions the predicted velocity gradient at the channel base is steeper as expected. However, the general trends in the variation of wall shear stress and boundary layer thickness are found to be the same. Thus, we do not expect any drastic differences in the solution trends by the use of a comprehensive turbulence model. As for the free surface behavior, the wall boundary conditions have only a minor effect. This is to be expected because the free surface is located sufficiently far from the boundary layer and thus the wall effects are not significant. The excellent agreement be-

$Re_H = 19\,685$, $H/L = 0.056$, $x_0 = 0.944$, $Q = 2.5\text{E-}4\ \mathrm{m^3\,s^{-1}}$

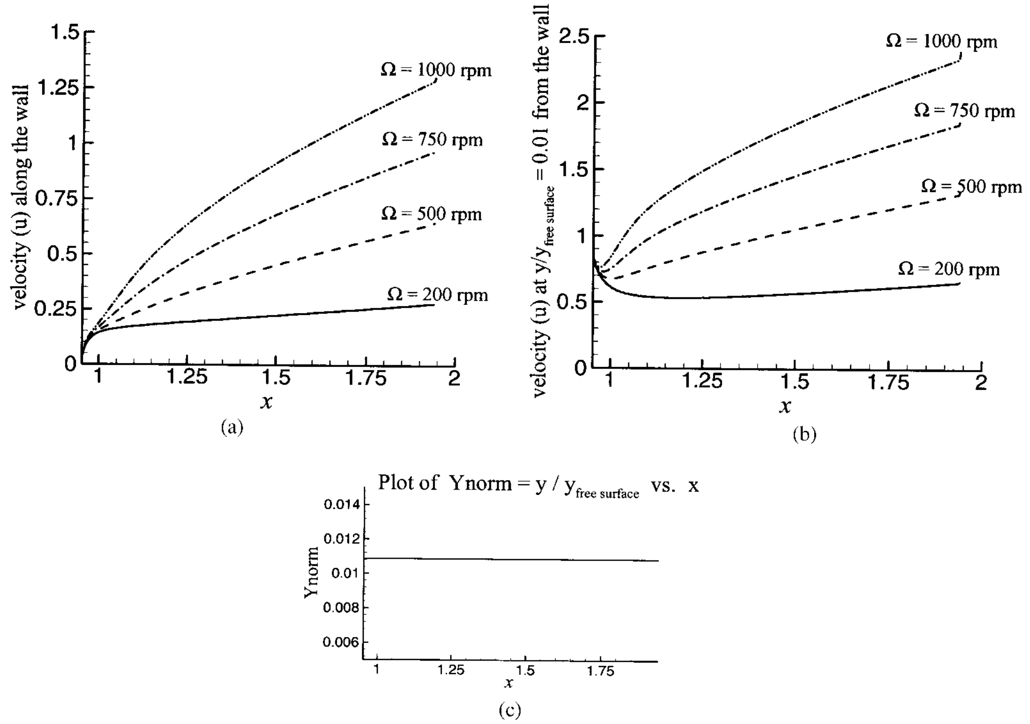

Figure 13. Effect of angular velocity on the streamwise velocity at (a) $y = \Delta y$, (b) $y/y_{fs} = 0.01$. In (c), the ratio y/y_{fs} is shown for the nodes adjacent to the wall.

tween the inviscid and the turbulent solutions near the free surface is further confirmation of this fact.

Thus even with our present turbulence model, we expect the results to be accurate for most part except, perhaps, in a region very near the wall.

We have taken special care to see that the solutions obtained in the present study are justified by rigorous mesh refinement tests. In addition, the solutions are physically meaningful.

It is true that some experimental data for free surface flow in rotating channel could be an added strong validation of the present results. However, such experimental data are not available in the open literature. Detailed experiments in such environments would demand excellent facilities, which only a few good laboratories could afford. Indeed, such an experimental setup and the results from it would form a topic on their own, capable of leading to independent publication. We consider our present computational effort as an important part of the overall problem of free surface turbulent flow modeling in a rotating channel.

On the positive side, wear experiments are conducted [5] routinely using the Coriolis wear tester. Invariably it is found [15, 21] that the sliding wear rate increases with distance along

$Re_H = 19\ 685$, $H/L = 0.056$, $x_0 = 0$, Q=2.5E-4 m^3 s^{-1}

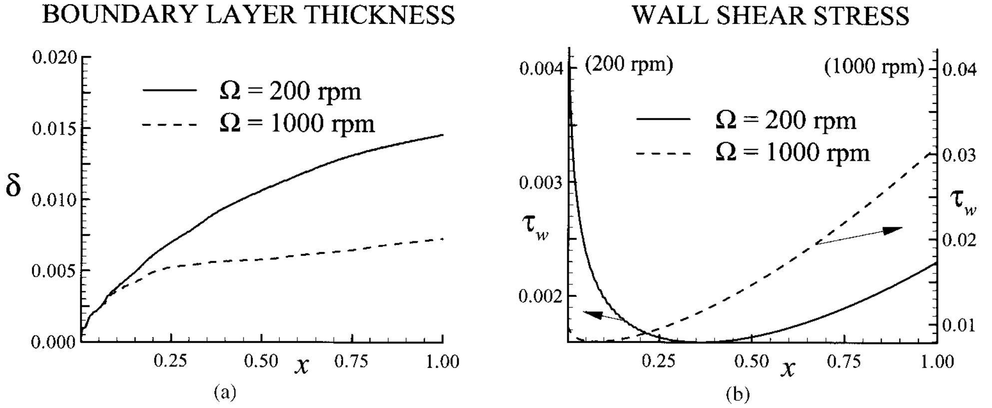

Figure 14. Comparison of turbulent boundary layer properties for $\Omega = 200$ rpm and $\Omega = 1000$ rpm respectively.

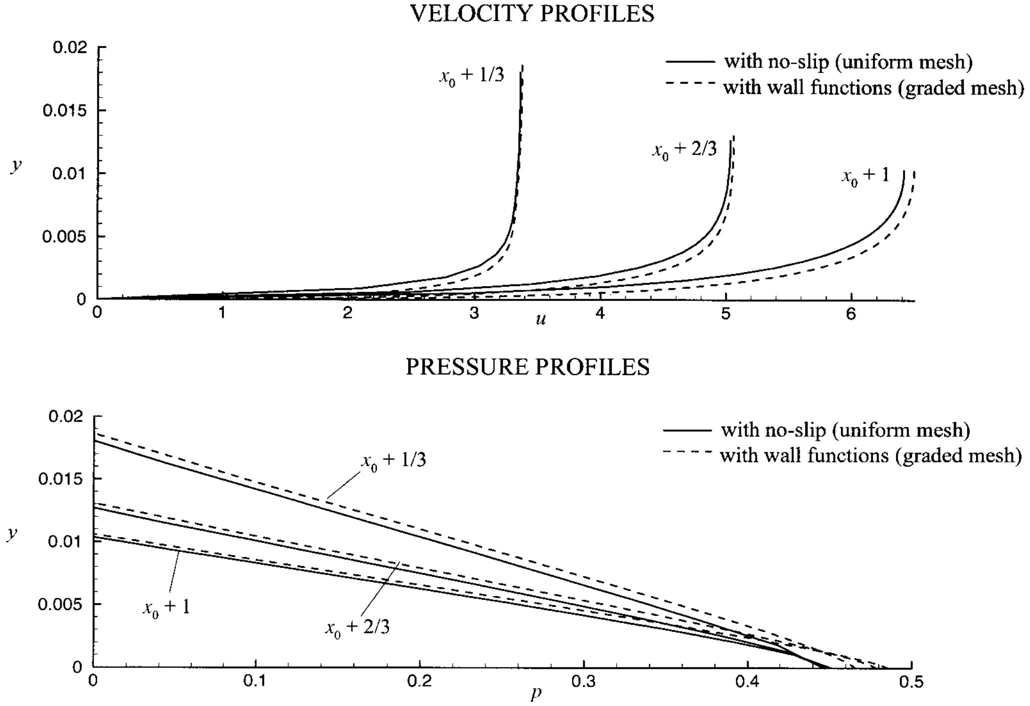

Figure 15. Comparison of velocity and pressure profiles for wall functions and no-slip along $y = 0$.

the channel base. The present single-phase flow results show that both the wall shear stress and the near-wall velocity increase along the channel base, confirming strongly the empirical evidence of increasing wear.

The predicted wear has been quantified by us by two-phase flow and erosion computations for the rotating channel [21]. The prediction methodology and details of these results are to appear shortly in a separate paper. We find a striking match between the numerical predictions and the experimental observations of wear rate.

NOMENCLATURE

English

a_i	Free surface parameters or coefficients in Hermite interpolation
H	Height of the channel
H_i	Hermite polynomials
$\underset{\sim}{I}$	Identity tensor
$\tilde{J}$	Jacobian of the transformation $(x, y) \rightarrow (\xi, \eta)$
L	Channel length
$\hat{n}$	Unit normal to the free surface
N_i	Biquadratic interpolating functions
N_{p_i}	Bilinear interpolating functions for pressure p
p	Pressure
Q	Volumetric flow rate or Jacobian matrix defined in Equation (20)
$\vec{r}$	Position vector
r_w	Wall roughness
Ro	Rossby number
Re	Length-based Reynolds number
Re_H	Height-based Reynolds number
$R_{u_i}, R_{v_i}, R_{p_i}, R_{a_i}$	Galerkin Residuals defined in Equations (15)–(17)
$\underset{\sim}{R}$	Vector of the Galerkin residuals
$\tilde{S}$	Height of the free surface
$\vec{u}$	Velocity vector
u	x-component of the velocity
U_0	Inlet velocity
v	y-component of the velocity
$\underset{\sim}{X}$	Vector of nodal values of u, v, p and free surface parameters a

Greek

α	Constant in Equation (4)
β	Parameter in Equation (9a)
Γ	Element boundary
η	Ordinate of normalized coordinate system
μ	Laminar viscosity
μ_t	Eddy viscosity
v_r	Ratio of eddy viscosity to laminar viscosity
ρ	Density of the incompressible liquid
$\underset{\sim}{\tau}$	Stress tensor

Ω	Angular velocity
ξ	Abscissa of normalized coordinate system

Subscripts

e	Pertaining to an element
i, j, k	Dummy indices
n	Component normal to the free surface
t	Component tangential to the free surface
τ	Friction velocity

Superscripts

$*$	Non-dimensional quantity
$+$	Non-dimensional quantity involving u_τ

REFERENCES

1. Saito H, Scriven LE. Study of coating flow by the finite element method. *Journal of Computational Physics* 1981; **42**:53–76.
2. Engelman MS, Sani RL. Computation techniques for fluid flow. *Recent Advances in Numerical Methods in Fluids*, Taylor C. *et al.* (eds). Vol. 5, Pincridge Press: Swansea, U.K., 1986; 47–74.
3. Veeraraghavan R, Pagalthivarthi KV. Solution methods for free surface flows: recent advances and case study. *Proceedings of the 24th National Conference on Fluid Mechanics and Fluid Power*, Bengal Engg College, Calcutta, Dec. 26–28, 1997, pp. D27–34,1997.
4. Tuzson JJ, Scheibe-Powell KA. Slurry erosion tests with centrifugal erosion tester. *Liquid–Solid Flows and Erosion Wear in Industrial Equipment*, *ASME-FED*, Roco MC (ed.). Vol. 13, pp. 84–87, 1984.
5. Pagalthivarthi KV, Helmly FW. Applications of materials wear testing to solids transport via centrifugal slurry pumps. *Wear Testing of Advanced Materials*, *ASTM STP 1167*. Divakar R, Blau PJ. (eds). pp. 114–126, 1992.
6. Majumdar AK, Pratap VS, Spalding DB. Numerical computation of flow in rotating ducts. *ASME Journal of Fluids and Engineering* 1977; **99**:148–153.
7. Majumdar AK, Spalding DB. Numerical investigation of three dimensional flows in a rotating duct by a partially parabolic procedure. ASME, paper 77-WA/FE-7, 1977.
8. Howard JHG, Patankar SV, Bordynuik RM. Flow prediction in rotating ducts using Coriolis-modified turbulence models. *ASME Fluids Engineering Division Winter Annual Meeting*, November 10–12, 1980, Chicago, IL. Paper No. 80-WA FE-1, 1980.
9. Younis BA. Prediction of turbulent flows in rotating rectangular ducts. *Transactions of the ASME*, *FED*, vol. 115, December, pp. 646–652, 1993.
10. Johnston JP, Halleen RM, Lezius DK. Effects of spanwise rotation on the structure of two-dimensional fully developed turbulent channel flow. *Journal of Fluid Mechanics* 1992; **56**(3):533–557.
11. Wagner RE, Velkoff HR. Measurements of secondary flows in a rotating duct. *ASME Journal of Engineering for Power* 1972; **94**:261–270.
12. Pagalthivarthi KV, Desai PV, Addie GR. Particulate motion and concentration fields in centrifugal slurry pumps. *Particulate Science and Technology* 1990; **8**:77–96.
13. Ettouney MH, Brown RA. Finite element methods for steady solidification problems. *Journal of Computational Physics* 1983; **49**:118–150.
14. Pagalthivarthi KV, Desai PV. Deforming finite element method for two moving boundary problems. *Proceedings of Conference on Numerical Methods in Thermal Problems*, Swansea, U.K., 1989.
15. Pagalthivarthi KV, Veeraraghavan R, Visintainer RJ. Finite element prediction of free surface flow in Coriolis wear tester. *Proc. FEDSM'98*, *ASME Fluids Engg Division Summer Meeting*, June 21–25, Paper no: FEDSM 98-5231, 1998.
16. Roco MC, Reinhardt E. Calculation of solid particle concentration in centrifugal impellers using finite element technique. *Proc. Hydrotransport 7 Conf.*, *BHRA*, pp. 359–376, 1980.
17. Ferziger JH, Peric M. *Computational Methods for Fluid Dynamics*. Springer-Verlag: New York, 1996.

18. Minemura K, Uchiyama T. Three-dimensional calculation of air–water two-phase flow in centrifugal pump impeller based on a bubbly flow model. *Transactions of the ASME*, *Journal of Fluids and Engineering* 1993; **115**:766–781.
19. Bradshaw P. The analogy between streamline curvature and buoyancy in turbulent shear flow. *Journal of Fluid Mechanics* 1969; **36**(1):171–191.
20. Koyoma H, Masuda S, Ariga L, Watanabe I. Stabilizing and destabilizing effects of Coriolis force on two-dimensional laminar and turbulent boundary layers. *ASME Journal for Engineering for Power* 1979; **101**(1): 23–31.
21. Ramanathan V. Prediction of two-phase free surface flow in rotating channels. *Ph.D. thesis*, submitted to Indian Institute of Technology, Delhi, 2000.
22. Hood P. Frontal solution program for unsymmetric matrices. *International Journal of Numerical Methods in Engineering* 1976; **10**:379.
23. Hoffman KA. *Computational Fluid Dynamics for Engineers*. (Engng. Edu. Sys.), 1989.
24. Tuzson JJ, Clark HM. The slurry erosion process in the Coriolis wear tester. *Proc. FEDSM'98*, *ASME Fluids Engg. Division Summer Meeting.* June 21–25, 1998, Washington, DC, paper no. FEDSM98-5144, 1998.